RESEARCH ARTICLE | MARCH 13 2023

## MesoTIRF: A prism-based Total Internal Reflection Fluorescence illuminator for high resolution, high contrast imaging of large cell populations

S. Foylan : W. B. Amos; J. Dempster; ... et. al



Appl. Phys. Lett. 122, 113701 (2023) https://doi.org/10.1063/5.0133032





CrossMark

### Articles You May Be Interested In

A dual beam total internal reflection fluorescence spectrometer for dynamic depth resolved measurements of biochemical liquid-solid interface binding reactions in opaque solvents

Rev Sci Instrum (September 1991)

Ultrastable combined atomic force and total internal fluorescence microscope

Rev Sci Instrum (June 2009)

Microplate-compatible total internal reflection fluorescence microscopy for receptor pharmacology

Appl. Phys. Lett. (May 2013)





# MesoTIRF: A prism-based Total Internal Reflection Fluorescence illuminator for high resolution, high contrast imaging of large cell populations

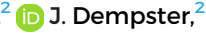
Cite as: Appl. Phys. Lett. 122, 113701 (2023); doi: 10.1063/5.0133032 Submitted: 1 November 2022 · Accepted: 28 February 2023 · Published Online: 13 March 2023 · Corrected: 20 March 2023























### **AFFILIATIONS**

- Department of Physics, University of Strathclyde, Glasgow G4 ONG, United Kingdom
- $^2$ Strathclyde Institute for Pharmacy & Biomedical Sciences, University of Strathclyde, Glasgow G4 0RE, United Kingdom
- <sup>3</sup>Centre for Inflammation Research, University of Edinburgh, Edinburgh EH16 4TJ, United Kingdom
- <sup>4</sup>Institute for Regeneration and Repair, University of Edinburgh, Edinburgh EH16 4UU, United Kingdom
- <sup>5</sup>Department of Chemical and Biological Sciences, National Physical Laboratory, Teddington TW11 OLW, United Kingdom
- <sup>6</sup>Department of Computer Science, University College London, London WC1E 6BT, United Kingdom

Note: This paper is part of the APL Special Collection on Advances in Optical Microscopy for Bioimaging.

<sup>a)</sup>Author to whom correspondence should be addressed: shannan.foylan@strath.ac.uk

#### **ABSTRACT**

Total Internal Reflection Fluorescence (TIRF) illumination bypasses the axial diffraction limit of light by using an evanescent field to excite fluorophores close to a sample substrate. However, standard TIRF imaging through the objective requires a high numerical aperture (NA) to generate the evanescent wave. Available lenses have a high magnification with a correspondingly small field of view—ranging from ~50  $\mu$ m to 1 mm in diameter. Switching to the older prism-TIRF configuration introduced by Axelrod in the 1980s might seem to remove the requirement for high objective NA and allow the use of existing large-field objectives. Unfortunately, these lenses are unsuitable because their throughput of light is too low for TIRF imaging. As such, high sensitivity TIRF imaging over a much larger mesoscopic field has yet to be demonstrated. We have developed a prism-based TIRF illuminator for the Mesolens—a highly corrected objective lens with an unparalleled ratio of NA to magnification. The imaging field of the Mesolens is 204 times larger than that of the TIRF objectives previously described, increasing the optical throughput of the optical system by a factor of 25 compared to an off-the-shelf microscope objective of the same magnification. We demonstrate MesoTIRF imaging of cell specimens and show the multi-wavelength capability of the modality across more than 700 cells in a single image.

© 2023 Author(s). All article content, except where otherwise noted, is licensed under a Creative Commons Attribution (CC BY) license (http:// creativecommons.org/licenses/by/4.0/). https://doi.org/10.1063/5.0133032

Total Internal Reflection Fluorescence (TIRF) microscopy is an established imaging technique in cell biology. It relies on delivering excitation light such that it is incident on a refractive index boundary at the microscope specimen plane above the characteristic critical angle necessary for total internal reflection (TIR). This phenomenon results in a rapidly decaying evanescent field that penetrates to a depth on the order of 100 nm. Such illumination allows structure below the axial diffraction limit to be visualized with high contrast while minimizing photobleaching of the specimen by reducing the illumination volume. TIRF microscopy has extensively been used in cell biology to image cell contacts<sup>1</sup> and study cell adhesion,<sup>2-4</sup> ion channels,<sup>5</sup> endocytosis, and the self-assembly of filamentous proteins. Generating TIR

at the specimen plane can be achieved using a TIRF objective, a waveguide, or a prism. To support super-critical illumination, TIRF objectives have a numerical aperture (NA) between 1.45 and 1.5 with associated high magnification factors of 60× or 100×. As such, the field of view (FOV) of the microscope system is restricted to between 50 and 350  $\mu m$  diameter imaging fields, and only a few cells can be viewed in a single image. 10 Stitching and tiling methods can be used to image larger specimen areas, but these methods are time-consuming and routinely introduce artifacts into the resultant image. Waveguidebased TIRF obviates the need for high NA objective lenses, allowing for images up to 0.5 mm in diameter containing tens of cells using custom-designed chips 10,11 to be obtained. Prism-based TIRF uses offthe-shelf components, is easier to implement than other methods and, like waveguide TIRF, is compatible with any objective lens. This potentially allows for larger FOV imaging than possible with TIRF objectives. However, for both waveguide and prism-based TIRF, the detection objective lens remains a fundamental limitation when considering FOV. Low magnification objective lenses that support wide FOV imaging typically have a low NA, which in turn leads to low lateral resolution images.

Here, we report MesoTIRF—prism-based TIRF mesoscopy using the Mesolens for imaging over a large FOV with high lateral and axial resolution. The Mesolens<sup>12</sup> combines low magnification with a high numerical aperture (4×/0.47 NA), and our dual-wavelength MesoTIRF illuminator generates an evanescent wave to cover the full observable FOV (4.4 mm × 3.0 mm). The field number of the Mesolens is 24, yielding the full imaging field of  $6 \text{ mm} \times 6 \text{ mm}$ . However, this field is truncated slightly in widefield to 4.4 mm × 3.0 mm due to limitations of the camera. One would require a 400 Mpixel camera in order to Nyquist sample the full 6 mm diameter field. Throughout this work, we refer to the measured "optical throughput" of our system over similar terms, such as étendue, optical invariant, and light gathering power. The optical throughput is a characteristic property of a lens that is the product of the pupil area and the collection angle of this pupil.<sup>13</sup> The optical throughput of the Mesolens has previously been reported as 25× that of a comparable magnification microscope objective, allowing for substantially improved light collection efficiency over the large FOV afforded by the low magnification. The optical performance of this unique mesoscopic imaging objective has been discussed thoroughly in

previous publications.<sup>12,14</sup> We present details of the optical setup and show the utility of MesoTIRF for high-contrast, high-resolution imaging of fluorescently labeled proteins in fixed cells. It is notable here that throughout this work we will refer to the benefits and attributes measured from the MesoTIRF modality. The authors are aware that the same benefits and attributes are true of conventional TIRF systems, but not on the scale reported here.

A schematic diagram of the optical set-up is shown in Fig. 1. The illumination laser source was a tunable wavelength (Chameleon Ultra II, Coherent) titanium sapphire laser pumping an optical parametric oscillator (OPO) (Compact OPO-Vis, Coherent). The second harmonic of the signal wavelength output of the OPO was used as the laser source, with 500 nm and 585 nm selected for dual-wavelength TIRF imaging. This choice of wavelengths was informed by the specification of the custom 100 mm diameter Pinkel-type  $^{15,16}$  chromatic reflector and barrier filters used for Mesolens imaging that allows fluorophore excitation/emission combinations of  $505\pm25\,\mathrm{nm}/542.5\pm7.5\,\mathrm{nm}$  and  $575.5\pm22.5\,\mathrm{nm}/677.5\pm72.5\,\mathrm{nm}$ . For comparison of the performance of the MesoTIRF illuminator with widefield epi-fluorescence illumination (WF epi), we used 504 (bandwidth = 19.4 nm) and 584 nm (bandwidth = 27 nm) light emitting diodes for wide-field illumination (pE-4000, CoolLED).

The optical power of the OPO SHG output beams at the specimen plane were adjusted using a combination of a polarizing beam splitter cube and a variable neutral density filter wheel. Next, the beam was expanded by a Keplerian telescope consisting of 50 and 100 mm focal length plano–convex lenses (anti-reflection coated for 350–700 nm). A first surface reflector in a kinematic mount was used

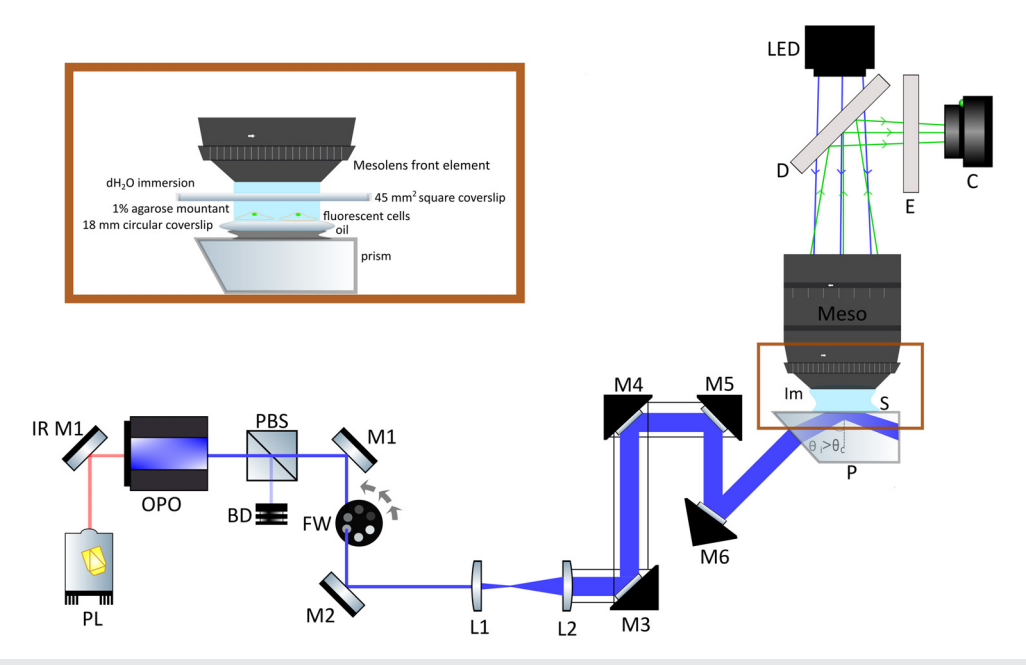


FIG. 1. Schematic of MesoTIRF. PL: titanium sapphire pump laser (Ultra II, Coherent); IR M1: infrared mirror (BB1-E03, Thorlabs); OPO: optical parametric oscillator (Chameleon OPO-Vis, Coherent); PBS: polarizing beam splitter (CCMS-PBS201/M, Thorlabs); BD: beam dump; M1-6: visible broadband dielectric mirrors (Thorlabs, BB1-E01); FW: filter wheel with five neutral density filters (Thorlabs, FW1A); L1: 50 mm plano-convex lens (LA1131-A-ML, Thorlabs); L2: 100 mm plano-convex lens (LA1509-A-ML, Thorlabs); M3-6 mounted in right angled cage mounts (KCB1C/M, Thorlabs); P: 45° borosilicate glass prism (Mesolens Ltd.); S: sample; Im: immersion fluid (distilled water); Meso: Mesolens objective element, D: dichroic filter; E: emission filter (custom from Chroma); C: chip-shifting camera sensor (VNP-29MC; Vieworks); LED: 504 and 584 nm LEDs from the LED module (pE-4000, CoolLED). Inset: illustration of the specimen mounting procedure for MesoTIRF imaging.

to adjust the angle of incidence of the beam to  $86^\circ$  at the top surface of a  $45^\circ$  borosilicate glass dove prism that served as the MesoTIRF prism. The theoretical evanescent field depth for a wavelength of 504 nm in a borosilicate prism (n = 1.51) at this incidence angle is 56 nm. The 25 mm thick prism has a top surface of  $20 \times 70$  mm and was placed on top of a computer-controlled specimen stage (ProScan III, Prior Scientific) for accurate positioning of the prism in three dimensions. To capture the large, high-resolution images produced by MesoTIRF, we used a chip-shifting camera sensor (VNP-29MC; Vieworks), which records images by shifting a 29-megapixel CCD chip in a  $3 \times 3$  array. Reconstruction of each image (260 Megapixels, 506 MB) took approximately 5 s on a typical computer workstation.

To confirm evanescent illumination, we prepared a specimen of murine fibroblast cells (3T3-L1) labeled with both a fluorescent nuclear marker (SYTO Green) and an antibody labeling against paxillin, a focal adhesion component.<sup>19</sup> We hypothesized that the fluorescent emission from the nuclear marker would be visible in WF epi but with MesoTIRF the cell nucleus would be too far above the basal membrane to be excited by the evanescent wave. To image the SYTO Green stain, the camera exposure time and the camera gain were set to 2 s and 1×, respectively, for both WF epi and MesoTIRF. In WF epi, the 504 nm LED power was adjusted to 25 mW to excite fluorescence from the stained nuclei without saturation. For MesoTIRF, the maximum available laser power at the specimen plane of 3.48 mW was used at a wavelength of 500 nm. To image the antibody against paxillin that was conjugated to Alexa Fluor Plus 594, the camera exposure time and the camera gain were set to 2 s and 70×, respectively, for both WF epi and MesoTIRF. The optical powers of the 584 nm LED (22 mW) and the 585 nm laser (3.48 mW) were adjusted to produce images of the fluorescently labeled paxillin with a similar fluorescence signal intensity. To estimate the number of cells, the "Surfaces" model in Imaris (Imaris 9.8, Oxford Instruments) was used for object detection of SYTO Green labeled nuclei in the WF epi image.

A comparison of signal-to-background ratio (SBR) in WF epi and MesoTIRF from this dual labeled sample was obtained by taking line intensity profiles in ImageJ<sup>20</sup> through three neighboring focal adhesions in the images from each modality. Following transfer of these data to Python, the peaks of each line profile where detected using the find\_peaks() function in the SciPy<sup>21</sup> library and scaled against the minimum signal intensity.

To evaluate the capability of MesoTIRF for dual-wavelength imaging including an assessment of the uniformity of illumination, a fixed HeLa cell specimen was prepared, using an anti-paxillin antibody conjugated to the fluorescent secondary antibody Alexa Fluor Plus 594 and fluorescein phalloidin that stains F-actin. For each sequential image, an exposure time of 2 s and a camera gain of  $30\times$  was used.

To evaluate the improvement in SBR in MesoTIRF compared with WF epi, the same specimen was imaged but only the anti-paxillin conjugated to Alexa Fluor Plus 594 was excited. To measure the SBR, the machine learning algorithm collection Trainable Weka<sup>22</sup> in ImageJ was used to identify and segment fluorescent objects from both WF epi and MesoTIRF images. A selection mask was extracted from this segmentation, which enabled us to derive the mean detected signal in a cell from the raw images using ImageJ.<sup>20</sup> The background signal was calculated for each image by selecting three background regions of interest, calculating the mean intensity, and averaging these measurements. This workflow was carried out for six ROIs separated by at least

0.5 mm across the full FOV to evaluate variations in SBR, and the uniformity of illumination.

To demonstrate MesoTIRF in another cell type, the human mesothelial cell line MeT-5A was fixed and labeled with antibodies against paxillin and tubulin, which were conjugated to Alexa Fluor 488 and Alexa Fluor Plus 594, respectively. These (adhesion and cytoskeletal) proteins are within the reach of an evanescent field. These dataset is included in the supplementary material.

Cell culture, fluorescent labeling, and specimen preparation methods are included in the supplementary material alongside quantification of focal adhesions imaged under WF epi and MesoTIRF.

Figure 2 shows a comparison of WF epi and MesoTIRF images of dual-labeled fixed 3T3-L1 cells prepared with fluorescent staining for nuclei (green) and paxillin (magenta). The full FOV WF epi image is shown in Fig. 2(a), with a region of interest (ROI) indicated by a yellow box that is digitally zoomed in 2B. Figure 2(c) shows the same area of the specimen imaged using dual-wavelength MesoTIRF, with the same ROI expanded in 2D.

Using WF epi, the cell nuclei are clearly visible in Fig. 2(b). These nuclei disappear, as expected, when imaged with MesoTIRF as shown in 2D, thus confirming that the evanescent wave in MesoTIRF is restricted to a shallow depth close to the coverslip and does not penetrate sufficiently deep into the sample to excite fluorescence from the labeled nuclei. Nonspecific binding or binding of the anti-paxillin antibody to cytosolic protein is apparent when imaged with WF epi, but this fluorescence signal also disappears when using MesoTIRF illumination. This is further evidenced by the intensity profiles through two neighboring nuclei [Fig. 2(e)] and through three neighboring focal adhesions [Fig. 2(f)] for both the WF epi image (teal) and MesoTIRF (dark red). The difference in background is clearly evident, with MesoTIRF yielding a 4.2-fold reduction in background through the neighboring focal adhesions over WF epi, with a less noisy baseline than that of the WF epi image. While the focal adhesions are still visible in WF epi, the contrast enhancement afforded by MesoTIRF allows for the elongated features to be easily distinguished from background. An SBR improvement of 4.84×/3.9×/3.87× was observed in focal adhesions 1, 2, and 3 [measured from peaks in Fig. 2(f) left to right], respectively, when switching from imaging with WF epi to MesoTIRF.

Furthermore, there is negligible nuclear signal in the MesoTIRF image [Fig. 2(e)] because, as discussed previously, the 86° incident beam (resulting in a calculated evanescent field depth of 56 nm) does not penetrate the cell specimen deep enough to excite the nuclear stain. Using the Imaris based "Surfaces" feature in the nuclear channel, 743 cells were counted in this single image. For the purposes of presentation, each image presented in Fig. 2 underwent the "Contrast Limited Adaptive Histogram Equalization (CLAHE)" local contrast adjustment function in ImageJ. <sup>20</sup> However, all analysis has been performed on raw image data.

The application of MesoTIRF for imaging of dual-labeled specimens is shown in Fig. 3. Figure 3 shows a  $4.4\,\mathrm{mm} \times 3.0\,\mathrm{mm}$  FOV dual-color MesoTIRF image, following application of CLAHE, with focal adhesions in magenta and F-actin in cyan. Yellow boxes show digitally zoomed images of six separate ROIs separated by a minimum distance of 0.5 mm. In all images, focal adhesions and the F-actin network adjacent to the basal cell membranes are clearly visible. We note that there is a less than a 50% decrease in fluorescence signal from the center to the

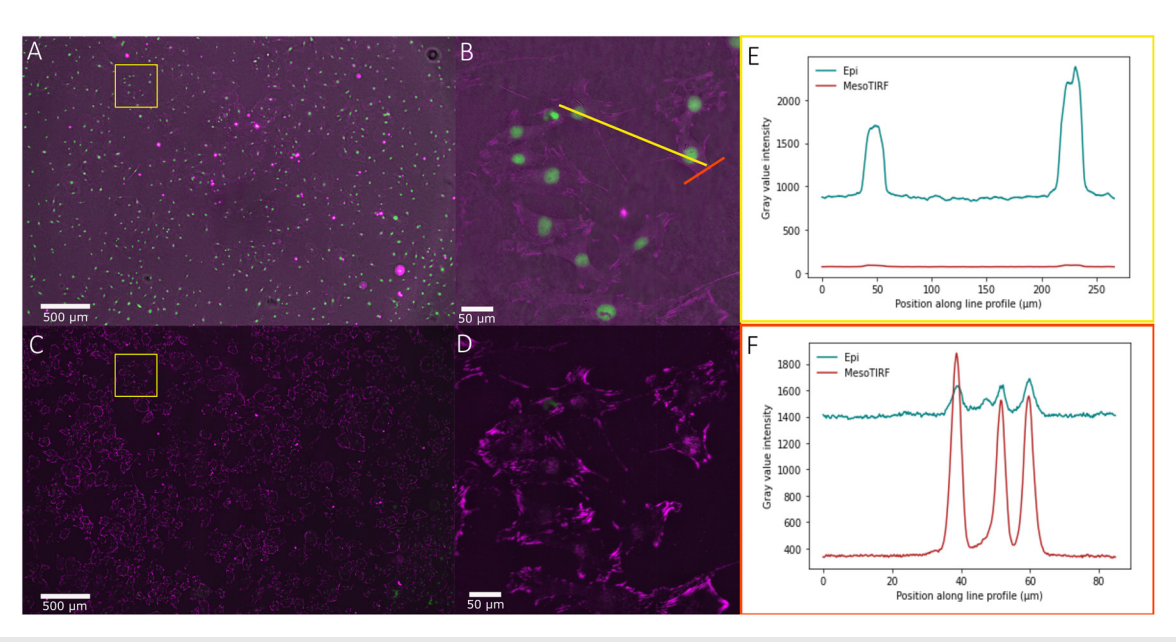


FIG. 2. Comparison imaging of WF epi and MesoTIRF: fixed 3T3-L1 cells labeled with SYTOGreen stain visualizing nuclei (shown in green) and with an anti-paxillin antibody conjugated to Alexa Fluor Plus 594 (shown in magenta). (a) WF epi image with 504 and 584 nm LEDs, (b) ROI digital zoom of (a) with line ROIs in yellow and orange to study nuclei and paxillin, respectively, (c) MesoTIRF image obtained with 500 and 585 nm OPO SHG illumination, (d) ROI digital zoom of (c), (e) yellow line profile intensity plot of neighboring nuclei in WF epi (teal) and MesoTIRF (dark red), and (f) orange line profile intensity for three neighboring focal adhesions in WF epi (teal) and MesoTIRF (dark red). Fluorescently labeled nuclei are visible in WF epi data but disappear when imaged with MesoTIRF. A considerable reduction image background signal is also observed in the MesoTIRF images.

edge of the imaged field, which we attribute to the Gaussian intensity profile of the illumination yielded from the optics chosen in Fig. 1.

Image quality analysis, quantification of resolvable detail with each illumination technique, and further MesoTIRF cell imaging is included in the supplementary material. Five line intensity profiles through neighboring fluorescent features imaged with WF epi and MesoTIRF served to measure the contrast improvement of MesoTIRF alongside providing topographical analysis of the focal adhesion features (Fig. S1). Uniformity of the MesoTIRF illuminator, using image data in Fig. 3, was quantified by counting the number of focal adhesions across six ROIs across the full image FOV (Fig. S2). Following on from this biological measure of uniformity, illumination uniformity was further examined using fluorescent test slides and measuring the cross section of each illumination technique with each utilized excitation wavelength (Fig. S3). Figure S4 shows a further example of two-color MesoTIRF imaging with the cell type MeT-5A labeled for paxillin and tubulin.

We have demonstrated MesoTIRF imaging of a range of different biological samples. Coupling a custom prism TIRF illuminator with the Mesolens<sup>12</sup> provides an unprecedented combination of a large FOV with high spatial resolution and high contrast image quality. The optical throughput of the Mesolens is 25 times greater than a commercial objective lens with a low magnification. This presents an advantage for MesoTIRF imaging, which enables lower optical power specimen illumination with corresponding reductions in photobleaching and phototoxicity. MesoTIRF utilized the comparatively cheap prism illumination method, allowing for ease when changing evanescent field depth by varying the incidence angle of the incident beam.

In our confirmation of TIRF illumination using the specimen that was dual-labeled with a nuclear stain and an antibody against the focal adhesion protein paxillin residing in the plasma membrane, we note that the position of the nuclei is dependent on where in their lifecycle the 3T3-L1 cells were at the point of formaldehyde fixation. However, we expect that the nuclear envelopes of each imaged cell was distal from the basal cell membrane, and therefore, outside the reach of an evanescent field from the MesoTIRF illuminator.

The ability of the MesoTIRF modality to capture fine details and the contrast improvement over WF epi was examined using a fixed mammalian cell line labeled for the focal adhesion component paxillin. Using the intensity signals through neighboring focal adhesions, an average 4.2-fold improvement in SBR was measured in MesoTIRF over WF epi, with the improvement in contrast allowing for more focal adhesions to be resolved with this novel modality (Fig. 2), while additionally yielding some topographical information (Fig. S1).

The dropoff in the intensity from the center to the edge of the MesoTIRF FOV was to be expected for an evanescent field generated using a Gaussian beam. This can be corrected either optically with beam shaping components to change the Gaussian profile to, for example, a top-hat, <sup>24</sup> or computationally, with algorithms, such as flat field correction, <sup>25</sup> a commonplace post-processing technique for many imaging modalities. However, as evident from the chosen ROIs in Fig. 3, the structural detail resolvable even in these dimmer peripheral areas remains of the quality expected of TIRF, with the same low background and individual punctate focal adhesions and spindled actin filaments that would be blurred by fluorescent signal excited from deeper in the cell in WF epi. A quantitative analysis of this uniformity, both from the biological specimen image provided in Fig. 3 and with a

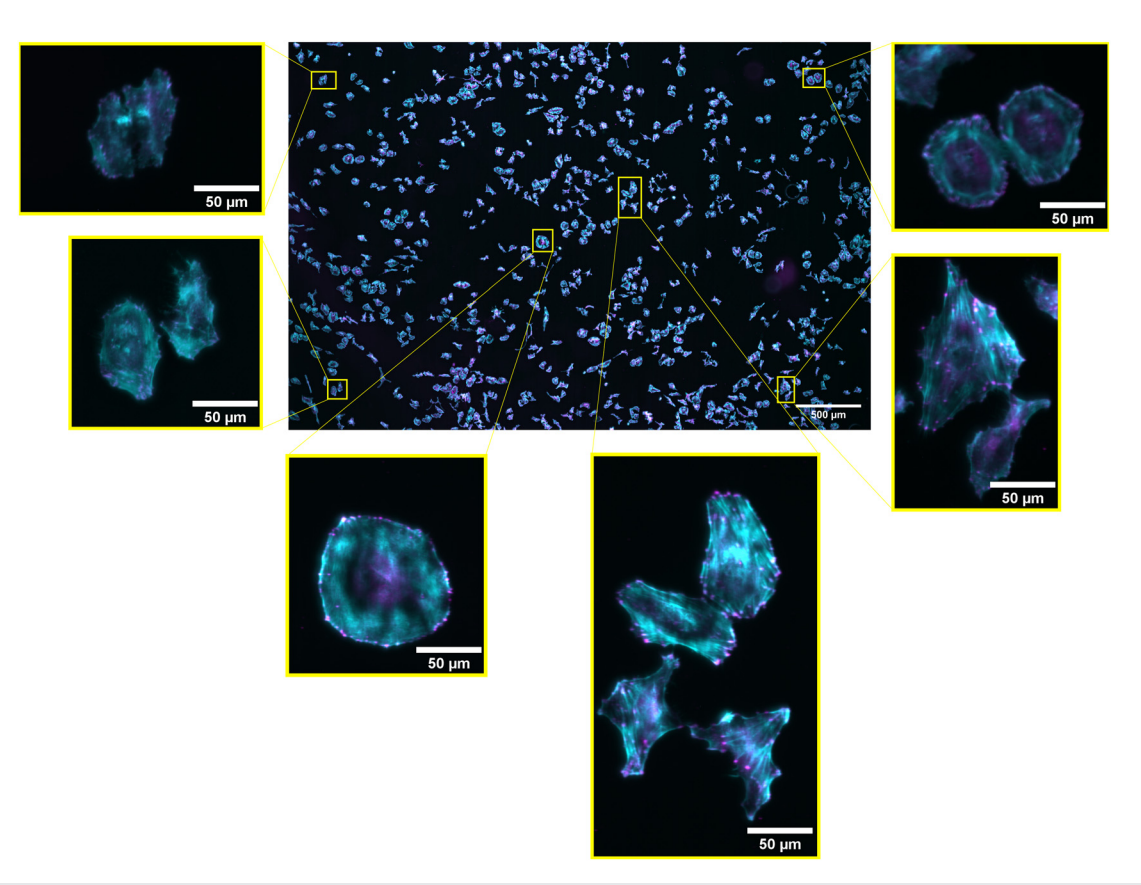


FIG. 3. Uniformity of MesoTIRF: fixed HeLa cells labeled with an anti-paxillin antibody conjugated to Alexa Fluor Plus 594 (magenta) and Fluorescein Phallodin, which stains the actin cytoskeleton (cyan). A full FOV MesoTIRF image is shown in the center with six ROIs indicated by yellow boxes. These show digital zoomed areas from the original dataset and confirm a small variation in the fluorescence intensity and little difference in the resolvable detail across the multi-millimeter FOV.

uniform non-biological test specimen, is included in the supplementary material (Figs. S2 and S3).

Excitation wavelengths for MesoTIRF are presently limited to the two discussed here by the large diameter Pinkel-type custom filters used for fluorescence detection. Additional custom filters would allow this to be extended for further wavelengths.

Mesolens data are rich in information, <sup>26</sup> but we recognize that an imaging rate of 0.2 Hz for MesoTIRF is insufficient for several applications *in vitro* such as cell signaling studies as reported by Crites *et al.*<sup>27</sup> However, with recent innovations in camera technologies, notably the development of cameras using large, high resolution 250 Mpixel sensors, such as the Canon 2U250MRXSAA CMOS sensor, tenfold higher imaging speeds (2.4 fps) can be achieved by avoiding the need for chip shifting. Additionally, sensor shifting technology has advanced in recent years, and a new sensor shifting camera providing a 604 MPixel image with a 1.5 fps imaging speed is now commercially available (VNP-604MX-MC-6-H, Vieworks). In combination with environmental control, this will offer opportunities to study faster dynamic processes, for example, the action of fast-acting antimicrobial peptides<sup>28</sup> or imaging of calcium transients in the plasma membrane.<sup>29</sup>

MesoTIRF may have applications in high-content screening <sup>10</sup> or wound healing models, <sup>30</sup> where large cell populations must be imaged to obtain statistically significant results. However, at present,

MesoTIRF is only compatible with imaging at room temperature, as there is no environmental imaging chamber that is compatible with the Mesolens. We are presently considering chamber designs that would be suitable for long-term imaging applications, including MesoTIRF.

A present limitation of MesoTIRF is the numerical aperture of the Mesolens; at 0.47, this is much lower than a typical TIRF lens, and, hence, the lateral resolution is around threefold poorer than that of a commercial objective TIRF microscope. With the principle of MesoTIRF now proven, one solution would be to increase spatial resolution using structured illumination, <sup>31,32</sup> introducing the possibility of super-resolution MesoTIRF-SIM. However, achieving SIM on the Mesolens is not trivial and would require either further optics in the MesoTIRF path to impose variable modulation patterns on the incident excitation beam or utilizing computational methods such as blind-SIM<sup>33</sup> algorithms. This would facilitate applications in single molecule localization microscopy in cell specimens approximately two orders of magnitude larger than current technology can image. At present, we are again limited by chip-shifting camera technology, but we are carefully following developments in this field.

See the supplementary material for cell specimen preparation, quantification of fine spatial detail visible under MesoTIRF illumination, quantification of the uniformity of the illumination, and additional cell membrane protein MesoTIRF imaging.

S.F. was supported by an iCASE award from the Engineering and Physical Sciences Research Council and the National Measurement System of the UK's Department for Business, Energy, and Industrial Strategy. L.K. was supported by the Engineering and Physical Sciences Research Council and the Medical Research Council (MRC) for Doctoral Training in Optical Medical Imaging (No. EP/L016559/1). The work ongoing in the Gram Hansen lab is supported by a University of Edinburgh Chancellor's Fellowship, Worldwide Cancer Research (No. 19-0238) and the June Hancock Mesothelioma Research Fund. M.S. is funded by the National Measurement System of the Department for Business, Energy, and Industrial Strategy. G.M. was supported by the Biotechnology and Biological Sciences Research Council (Nos. BB/P02565X/1 and BB/T011602/1) and the MRC (No. MR/K015583/1). Both G.M. and W.B.A. are partially supported by the Leverhulme Trust.

# AUTHOR DECLARATIONS Conflict of Interest

The authors have no conflicts to disclose.

#### **Author Contributions**

Shannan Foylan: Conceptualization (equal); Data curation (lead); Formal analysis (lead); Funding acquisition (supporting); Investigation (lead); Methodology (equal); Validation (equal); Visualization (equal); Writing - original draft (lead); Writing - review & editing (equal). William Bradshaw Amos: Methodology (equal); Visualization (supporting); Writing - original draft (supporting); Writing - review & editing (equal). John Dempster: Data curation (equal); Methodology (equal); Resources (equal); Software (lead); Visualization (equal); Writing - original draft (equal); Writing - review & editing (equal). Lisa Koelln: Conceptualization (equal); Methodology (equal); Writing - review & editing (equal). Carsten Gram Hansen: Conceptualization (supporting); Funding acquisition (equal); Project administration (equal); Resources (equal); Writing - review & editing (equal). Michael James Shaw: Conceptualization (equal); Funding acquisition (equal); Methodology (equal); Project administration (equal); Supervision (equal); Writing - original draft (equal); Writing review & editing (equal). Gail McConnell: Conceptualization (lead); Funding acquisition (lead); Methodology (lead); Project administration (lead); Resources (lead); Supervision (lead); Validation (equal); Writing original draft (equal); Writing - review & editing (equal).

#### DATA AVAILABILITY

The data that support the findings of this study are available within the article and its supplementary material.

#### **REFERENCES**

- <sup>1</sup>D. Axelrod, "Cell-substrate contacts illuminated by total internal reflection fluorescence," J. Cell Biol. **89**, 141–145 (1981).
- <sup>2</sup>M. C. D. Santos, C. Vézy, and R. Jaffiol, "Nanoscale characterization of vesicle adhesion by normalized total internal reflection fluorescence microscopy," Biochim. Biophys. Acta 1858, 1244–1253 (2016).
- <sup>3</sup>J. Oreopoulos and C. M. Yip, "Probing membrane order and topography in supported lipid bilayers by combined polarized total internal reflection fluorescence-atomic force microscopy," Biophys. J. **96**, 1970–1984 (2009).

- <sup>4</sup>A. E. Ward, V. Kiessling, O. Pornillos, J. M. White, B. K. Ganser-Pornillos, and L. K. Tamm, "HIV-cell membrane fusion intermediates are restricted by Serincs as revealed by cryo-electron and TIRF microscopy," J. Biol. Chem. 295, 15183–15195 (2020).
- <sup>5</sup>R. M. Luik, M. M. Wu, J. Buchanan, and R. S. Lewis, "The elementary unit of store-operated Ca<sup>2+</sup> entry: Local activation of CRAC channels by STIM1 at ER-plasma membrane junctions," J. Cell Biol. 174, 815–825 (2006).
- <sup>6</sup>M. J. Taylor, D. Perrais, and C. J. Merrifield, "A high precision survey of the molecular dynamics of mammalian clathrin-mediated endocytosis," PLOS Biol. 9, e1000604 (2011).
- <sup>7</sup>A. Bella, M. Shaw, S. Ray, and M. G. Ryadnov, "Filming protein fibrillogenesis in real time," Sci. Rep. 4, 7529 (2014).
- <sup>8</sup>H. M. Grandin, B. Städler, M. Textor, and J. Vörös, "Waveguide excitation fluorescence microscopy: A new tool for sensing and imaging the biointerface," Biosens. Bioelectron. 21, 1476–1482 (2006).
- <sup>9</sup>D. Axelrod, "Total internal reflection fluorescence microscopy in cell biology," Traffic (Copenhagen, Denmark) 2, 764–774 (2001).
- <sup>10</sup>D. A. Coucheron, Ø. Ivar Helle, C. I. Øie, J. C. Tinguely, and B. S. Ahluwalia, "High-throughput total internal reflection fluorescence and direct stochastic optical reconstruction microscopy using a photonic chip," J. Visual. Exp. 2019, e60378.
- <sup>11</sup>R. Diekmann, Ø. I. Helle, C. I. Øie, P. McCourt, T. R. Huser, M. Schüttpelz, and B. S. Ahluwalia, "Chip-based wide field-of-view nanoscopy," Nat. Photonics 11, 322–328 (2017).
- <sup>12</sup>G. McConnell, J. Trägårdh, R. Amor, J. Dempster, E. Reid, and W. B. Amos, "A novel optical microscope for imaging large embryos and tissue volumes with sub-cellular resolution throughout," eLife 5, e18659 (2016).
- <sup>13</sup>W. J. Smith, "Image formation: Geometrical and physical optics," in *Handbook of Optics* (McGraw-Hill, 1978).
- 14 R. Chhetri and P. Keller, "Microscopy: Imaging far and wide," eLife 5, e21072 (2016).
  15 D. Pinkel, J. Gray, R. Segraves, F. Waldman, B. Trask, L. C. Yu, D. Eastmond, and P. Dean, "Fluorescent nucleic acid hybridization methods," Proc. SPIE 1063, 123 (1989)
- 16-See https://www.semrock.com/multiband-filter-set-terminology.aspx for Multiband Filter Set Terminology.
- <sup>17</sup>D. Axelrod, "Evanescent excitation and emission in fluorescence microscopy," Biophys. J. **104**, 1401 (2014).
- <sup>18</sup>J. Schniete, A. Franssen, J. Dempster, T. J. Bushell, W. B. Amos, and G. McConnell, "Fast optical sectioning for widefield fluorescence mesoscopy with the mesolens based on HiLo microscopy," Sci. Rep. 8, 16259 (2018).
- C. E. Turner, J. R. Glenney, and K. Burridge, "Paxillin: A new vinculin-binding protein present in focal adhesions," J. Cell Biol. 111, 1059–1068 (1990).
   C. T. Rueden, J. Schindelin, M. C. Hiner, B. E. DeZonia, A. E. Walter, E. T.
- <sup>26</sup>C. T. Rueden, J. Schindelin, M. C. Hiner, B. E. DeZonia, A. E. Walter, E. T. Arena, and K. W. Eliceiri, "Image]2: Image] for the next generation of scientific image data," BMC Bioinf. 18, 529 (2017).
- <sup>21</sup>P. Virtanen, R. Gommers, T. E. Oliphant, M. Haberland, T. Reddy, D. Cournapeau, E. Burovski, P. Peterson, W. Weckesser, J. Bright, S. J. van der Walt, M. Brett, J. Wilson, K. J. Millman, N. Mayorov, A. R. Nelson, E. Jones, R. Kern, E. Larson, C. J. Carey, İ. Polat, Y. Feng, E. W. Moore, J. VanderPlas, D. Laxalde, J. Perktold, R. Cimrman, I. Henriksen, E. A. Quintero, C. R. Harris, A. M. Archibald, A. H. Ribeiro, F. Pedregosa, P. van Mulbregt, A. Vijaykumar, A. P. Bardelli, A. Rothberg, A. Hilboll, A. Kloeckner, A. Scopatz, A. Lee, A. Rokem, C. N. Woods, C. Fulton, C. Masson, C. Häggström, C. Fitzgerald, D. A. Nicholson, D. R. Hagen, D. V. Pasechnik, E. Olivetti, E. Martin, E. Wieser, F. Silva, F. Lenders, F. Wilhelm, G. Young, G. A. Price, G. L. Ingold, G. E. Allen, G. R. Lee, H. Audren, I. Probst, J. P. Dietrich, J. Silterra, J. T. Webber, J. Slavič, J. Nothman, J. Buchner, J. Kulick, J. L. Schönberger, J. V. de Miranda Cardoso, J. Reimer, J. Harrington, J. L. C. Rodríguez, J. Nunez-Iglesias, J. Kuczynski, K. Tritz, M. Thoma, M. Newville, M. Kümmerer, M. Bolingbroke, M. Tartre, M. Pak, N. J. Smith, N. Nowaczyk, N. Shebanov, O. Pavlyk, P. A. Brodtkorb, P. Lee, R. T. McGibbon, R. Feldbauer, S. Lewis, S. Tygier, S. Sievert, S. Vigna, S. Peterson, S. More, T. Pudlik, T. Oshima, T. J. Pingel, T. P. Robitaille, T. Spura, T. R. Jones, T. Cera, T. Leslie, T. Zito, T. Krauss, U. Upadhyay, Y. O. Halchenko, and Y. Vázquez-Baeza, "SciPy 1.0: Fundamental algorithms for scientific computing in Python," Nat. Methods 17, 261-272 (2020).
- <sup>22</sup>I. Arganda-Carreras, V. Kaynig, C. Rueden, K. W. Eliceiri, J. Schindelin, A. Cardona, and H. S. Seung, "Trainable Weka segmentation: A machine learning tool for microscopy pixel classification," Bioinformatics 33, 2424–2426 (2017).

- <sup>23</sup>M. Webster, K. L. Witkin, and O. Cohen-Fix, "Sizing up the nucleus: Nuclear shape, size and nuclear-envelope assembly," J. Cell Sci. 122, 1477–1486 (2009).
- <sup>24</sup>A. Möhl, S. Wickenhagen, and U. Fuchs, "Gauss to top-hat beam shaping with aspheres," Proc. SPIE 9741, 974102 (2016).
- <sup>25</sup> M. Model, "Intensity calibration and flat-field correction for fluorescence microscopes," Curr. Protoc. Cytom. 68, 10.14.1 (2014).
- <sup>26</sup>M. Shaw, R. Claveau, P. Manescu, M. Elmi, B. J. Brown, R. Scrimgeour, L. S. Kölln, G. McConnell, and D. Fernandez-Reyes, "Optical mesoscopy, machine learning, and computational microscopy enable high information content diagnostic imaging of blood films," J. Pathol. 255, 62–71 (2021).
- <sup>27</sup>T. J. Crites, L. Chen, and R. Varma, "A TIRF microscopy technique for real-time, simultaneous imaging of the TCR and its associated signaling proteins," J. Visual. Exp. 61, 3892 (2012).
- <sup>28</sup>A. K. Buck, D. E. Elmore, and L. E. Darling, "Using fluorescence microscopy to shed light on the mechanisms of antimicrobial peptides," Future Med. Chem. 11, 2447–2460 (2019).

- <sup>29</sup>P. Toglia, G. Ullah, and J. E. Pearson, "Analyzing optical imaging of Ca<sup>2+</sup> signals via TIRF microscopy: The limits on resolution due to chemical rates and depth of the channels," Cell Calcium 67, 65–73 (2017).
- 30S. Sen-Britain, D. M. Britain, W. L. Hicks, and J. A. Gardella, "TOF-SIMS and TIRF microscopy investigation on the effects of HEMA copolymer surface chemistry on spatial localization, surface intensity, and release of fluorescently labeled keratinocyte growth factor," Biointerphases 14, 051003 (2019).
- <sup>31</sup>P. Kner, B. B. Chhun, E. R. Griffis, L. Winoto, and M. G. Gustafsson, "Super-resolution video microscopy of live cells by structured illumination," Nat. Methods 6, 339–342 (2009).
- <sup>32</sup>J. Roth, J. Mehl, and A. Rohrbach, "Fast TIRF-SIM imaging of dynamic, low-fluorescent biological samples," Biomed. Opt. Express 11, 4008 (2020).
- <sup>33</sup>R. Ayuk, H. Giovannini, A. Jost, E. Mudry, J. Girard, T. Mangeat, N. Sandeau, R. Heintzmann, K. Wicker, K. Belkebir, and A. Sentenac, "Structured illumination fluorescence microscopy with distorted excitations using a filtered blind-SIM algorithm," Opt. Lett. 38(22), 4723–4726 (2013).